

Probing Neutron Skins with KDAR Neutrinos: From Coherent to Diffractive Elastic Neutrino–Nucleus Scattering

Kyoungsu Heo¹, Heesung Kwon¹, Jaewon Kim¹, Jubin Park^{1*}, Myung-Ki Cheoun^{1†}, Eunja Ha^{2‡}, Kyung Kwang Joo^{3§}

¹Department of Physics and Origin of Matter and Evolution of Galaxy (OMEG) Institute, Soongsil University, Seoul 06978, Korea

²Department of Physics and Research Institute for Natural Science, Hanyang University, Seoul 04763, Korea

³Center for Precision Neutrino Research (CPNR), Department of Physics, Chonnam National University, Yongbong-ro 77, Puk-gu, Gwangju 61186, Korea

February 23, 2026

Abstract

We investigate coherent elastic neutrino–nucleus scattering (CE ν NS) induced by pion–decay–at–rest (π DAR) and kaon–decay–at–rest (KDAR) neutrinos, with emphasis on the transition from strict coherence to the diffractive regime. Organizing CE ν NS observables in terms of the dimensionless variable qR , we show that π DAR measurements remain confined to the near-coherent region for all nuclei, whereas KDAR neutrinos ($E_\nu = 236$ MeV) extend the kinematics into $qR \gtrsim 1$, where recoil spectra develop genuine shape sensitivity to the nuclear weak form factor. Using representative light, medium–mass, and heavy nuclei (^{12}C , ^{40}Ca , ^{48}Ca , and ^{208}Pb), we examine relevant cross sections and quantify the statistical sensitivity to the neutron skin thickness achievable at a JSNS²–like facility. For a total exposure of 10 ton-year and realistic KDAR fluences, projected 1σ sensitivities reach $\Delta R_{np}^{(1\sigma)} \simeq 0.09\text{--}0.02$ fm for ^{48}Ca and $\simeq 0.07\text{--}0.02$ fm for ^{208}Pb as the fluence increases. These sensitivities are competitive with, and complementary to, parity–violating electron–scattering measurements such as CREX and PREX, while relying on an electroweakly clean neutral–current probe with distinct systematic uncertainties. Our results establish KDAR–based CE ν NS as a quantitatively robust and complementary avenue for probing neutron skins and nuclear weak densities beyond the coherent limit.

Keywords: Coherent elastic neutrino–nucleus scattering, Neutron skin, Weak form factors, Nuclear structure, KDAR neutrinos

1 Introduction

Coherent elastic neutrino–nucleus scattering (CE ν NS) is a neutral–current process in which a neutrino couples coherently to the weak charge of an entire nucleus. At sufficiently low momentum transfer, scattering amplitudes from individual nucleons add in phase, and the cross section scales approximately with the square of the weak charge, Q_W^2 . Because the proton contribution is strongly

*Corresponding author. E-mail: honolov@ssu.ac.kr

†Corresponding author. E-mail: cheoun@ssu.ac.kr

‡E-mail: ejaha@hanyang.ac.kr

§E-mail: kkjoo@chonnam.ac.kr

suppressed by the factor $1 - 4\sin^2\theta_W$ ¹, the weak charge is dominated by neutrons, yielding the characteristic scaling $Q_W^2 \simeq N^2$. CE ν NS therefore provides an electroweakly clean and theoretically controlled probe of neutron distributions and neutron skins in nuclei.

Early accelerator measurements of CE ν NS employed neutrinos from pion decay at rest (π DAR), which produce a prompt monoenergetic ν_μ at 29.8 MeV via $\pi^+ \rightarrow \mu^+ \nu_\mu$, followed by delayed $\bar{\nu}_\mu$ and ν_e from μ^+ decay. As a result, existing accelerator-based CE ν NS measurements probe neutrino energies around $E_\nu \simeq 30$ MeV. In contrast, kaon decay at rest (KDAR) provides a monoenergetic ν_μ with a substantially higher energy of 236 MeV through $K^+ \rightarrow \mu^+ \nu_\mu$. This increase in neutrino energy extends the accessible momentum-transfer and recoil ranges, opening sensitivity to nuclear weak-form-factor effects beyond the strictly coherent regime.

Since the first observation of CE ν NS with a CsI[Na] detector at the stopped-pion source of the Spallation Neutron Source (SNS) in 2017 [1], experimental studies have expanded rapidly across targets and neutrino sources. The COHERENT collaboration reported the first spectral measurement on argon in 2021 [2] and subsequently presented evidence for CE ν NS on germanium [3]. At reactor experiments, the CONUS+ collaboration reported a 3.7σ observation of CE ν NS in the sub-keV to keV recoil regime in 2025 [4]. In parallel, large liquid-xenon detectors developed for dark-matter searches have observed CE ν NS induced by solar ^8B neutrinos, with first signals reported by XENONnT and PandaX-4T in 2024 [5, 6].

Across these diverse experimental settings, CE ν NS measurements enable precision tests of the Standard Model at low momentum transfer, including determinations of the weak mixing angle that complement atomic parity violation and parity-violating electron scattering. They also provide direct sensitivity to neutron distributions through the weak form factor $F_W(q)$, allowing constraints on the neutron rms radius $R_n \equiv \sqrt{\langle r^2 \rangle_n}$ and the neutron skin thickness $\Delta R_{np} \equiv R_n - R_p = \sqrt{\langle r^2 \rangle_n} - \sqrt{\langle r^2 \rangle_p}$, where $R_p \equiv \sqrt{\langle r^2 \rangle_p}$ is the proton rms radius, once sufficient statistics are accumulated [7, 8]. Beyond nuclear structure, CE ν NS offers sensitivity to nonstandard neutrino interactions and other physics beyond the Standard Model through combined rate-and-shape analyses [9].

Despite this progress, the neutron skin thickness of medium and heavy nuclei remains a major open question. Recent parity-violating electron-scattering measurements report $\Delta R_{np}(^{48}\text{Ca}) = 0.121 \pm 0.026$ fm (CREX) and $\Delta R_{np}(^{208}\text{Pb}) = 0.283 \pm 0.071$ fm (PREX-II) [10, 11], while hadronic probes yield partially overlapping but not fully consistent results [12, 13]. The present experimental uncertainties, at the level of ~ 0.03 – 0.07 fm, map directly onto uncertainties in the density dependence of the nuclear symmetry energy and the pressure of neutron-rich matter in neutron stars [14]. An independent electroweak probe of the neutron density, subject to different and largely orthogonal systematic uncertainties, is therefore of considerable interest.

At low momentum transfer, the CE ν NS differential cross section is given by [15]

$$\frac{d\sigma}{dT} = \frac{G_F^2 M}{4\pi} Q_W^2 \left(1 - \frac{MT}{2E_\nu^2}\right) F_W(q)^2, \quad Q_W \simeq N - (1 - 4\sin^2\theta_W)Z, \quad (1)$$

showing that all nuclear-structure dependence enters through the weak form factor, the Fourier transform of the weak (primarily neutron) density. Here G_F is the Fermi constant, E_ν is the incident neutrino energy, T is the nuclear recoil kinetic energy, M is the nuclear mass, and Z (N) is the proton (neutron) number. The momentum transfer q is related to the recoil energy by

¹At the low momentum transfers relevant for CE ν NS, we adopt a low-energy effective weak mixing angle appropriate for neutral-current processes, $\sin^2\theta_W(Q^2 \simeq 0) = 0.2386$, which incorporates electroweak radiative corrections, including the running of $\sin^2\theta_W$, γ - Z mixing, and box-diagram contributions. This choice is suitable for momentum transfers $Q \sim \mathcal{O}(10\text{--}100)$ MeV. The value quoted at the Z pole, $\sin^2\theta_W^{\text{MS}}(m_Z) \simeq 0.231$, corresponds to a much higher energy scale and is therefore not directly applicable to CE ν NS processes.

$q = \sqrt{2MT}/(\hbar c)$ (see Sec. 2). Sensitivity to neutron radii and surface properties increases sharply as measurements extend from the strictly coherent regime ($qR \lesssim 1$) into the coherent-to-diffractive transition, where $F_W(q)$ departs from unity and develops a weak oscillatory structure.

Most existing CE ν NS measurements employing π DAR neutrinos remain confined to the near-coherent regime for all experimentally relevant nuclei, rendering recoil spectra only weakly sensitive to neutron-skin effects [7, 8]. In this work we show that KDAR neutrinos provide a qualitatively different kinematic reach. For medium and heavy nuclei, KDAR CE ν NS accesses the transition region $qR \gtrsim 1$ and, in the high-recoil tail, approaches the vicinity of the first diffractive minimum. Under JSNS² (J-PARC Sterile Neutrino Search at the J-PARC Spallation Neutron Source)-like benchmark conditions, this kinematic lever arm translates into projected statistical sensitivities reaching $\Delta R_{np}^{(1\sigma)} \sim 0.03\text{--}0.05$ fm for ⁴⁸Ca and $\sim 0.02\text{--}0.03$ fm for ²⁰⁸Pb with a total exposure of 10 ton-year, comparable to or improving upon current electroweak constraints from CREX and PREX-II. By combining analytic low- q benchmarks with full weak-form-factor calculations, we demonstrate how KDAR-induced recoil spectra can be exploited to extract neutron-skin information in a controlled and quantitative manner. These results establish KDAR CE ν NS as a powerful and complementary electroweak probe of neutron structure beyond the strictly coherent limit.

This paper is organized as follows. Section 2 introduces the weak form factor formalism employed in this work and summarizes the coherence condition and exact elastic kinematics used to map recoil observables onto the momentum transfer. Section 3 presents numerical results for representative targets, highlighting how KDAR extends CE ν NS from the near-coherent regime into the coherent-to-diffractive transition and how this affects recoil spectra. Section 4 develops a perturbative interpretation of neutron-skin sensitivity, connects variations of the weak form factor to variations of ΔR_{np} , and presents both the kinematic constraints and the JSNS²-based quantitative sensitivity estimates (see Tables 4 and 5). Finally, section 5 summarizes our findings and discusses their implications for future CE ν NS cross section and neutron-skin measurements.

2 Weak Form Factors, Coherence, and Kinematics in CE ν NS

The sensitivity of coherent elastic neutrino-nucleus scattering (CE ν NS) to nuclear structure is governed by the momentum transfer \mathbf{q} relative to the characteristic nuclear size R . Physically, coherence reflects the inability of the exchanged neutral weak boson to resolve spatial variations of the nuclear weak charge inside the nucleus. Throughout this work, we use the natural unit system, i.e., $\hbar = c = 1$. Then the three-momentum transfer q can be expressed in terms of the reduced wavelength of the exchanged boson,

$$\bar{\lambda}_{Z^0} \equiv \frac{\hbar c}{|\mathbf{q}|} = \frac{1}{q}, \quad (2)$$

such that coherent scattering occurs for $\bar{\lambda}_{Z^0} \gtrsim R$, equivalently $qR \lesssim 1$. In this regime, scattering amplitudes from different regions of the nucleus add coherently and the cross section exhibits the characteristic enhancement proportional to Q_W^2 . As qR increases beyond unity, spatial phases across the nuclear volume are no longer aligned, the weak form factor departs from unity, and CE ν NS becomes sensitive to the internal structure of the nucleus. This coherent-to-diffractive transition underlies the emergence of neutron surface and neutron-skin sensitivity.

For $qR \gg 1$, the momentum transfer is sufficiently large enough to resolve individual nucleons. In this limit, scattering amplitudes add incoherently and elastic coherence is lost, typically leading to inelastic processes. The cross section then scales approximately with the number of scattering centers rather than with the square of the weak charge. Between these two extremes lies an intermediate elastic regime, $qR \sim 1$, in which the nucleus recoils elastically but coherence is only partial. Here

the event rate is suppressed by the nuclear weak form factor, $|F_W(q)| < 1$, and sensitivity to nuclear structure begins to develop. This intermediate regime is of central importance for extracting neutron radii and neutron skins from CE ν NS data.

For spherically symmetric nuclei, the normalized nuclear weak form factor is defined as

$$F_W(q) = \frac{4\pi}{Q_W} \int_0^\infty r^2 \rho_W(r) j_0(qr) dr, \quad j_0(x) = \frac{\sin x}{x}, \quad (3)$$

where $\rho_W(r)$ denotes the weak-charge density and

$$Q_W \equiv \int d^3r \rho_W(r) = N - (1 - 4 \sin^2 \theta_W) Z \quad (4)$$

is the nuclear weak charge in the standard Freedman convention. With this normalization, the weak form factor satisfies $F_W(0) = 1$. The weak-charge density can be decomposed into neutron and proton contributions as

$$\rho_W(r) = \rho_n(r) - (1 - 4 \sin^2 \theta_W) \rho_p(r), \quad (5)$$

leading to

$$F_W(q) = \frac{N F_n(q) - (1 - 4 \sin^2 \theta_W) Z F_p(q)}{Q_W},$$

$$F_{n,p}(q) = \frac{1}{N(Z)} \int \rho_{n,p}(\mathbf{r}) \exp\left(i \frac{\mathbf{q} \cdot \mathbf{r}}{\hbar c}\right) d^3r. \quad (6)$$

Here $q \equiv |\mathbf{q}|$ is the corresponding wavenumber in fm^{-1} used as the form-factor argument. Because the proton contribution is strongly suppressed by the small factor $(1 - 4 \sin^2 \theta_W)$, CE ν NS observables are dominantly sensitive to the neutron distribution. As a result, the weak form factor closely tracks the neutron form factor, $F_W(q) \simeq F_n(q)$, up to a small and well-controlled correction.

In this work we employ two standard parametrizations of the nuclear weak density: the Helm model and the two-parameter Fermi (2pF) distribution. These phenomenological descriptions capture the essential bulk and surface features of neutron distributions relevant for CE ν NS, while remaining transparent and computationally efficient [16]. More microscopic approaches, such as DRHBc or Skyrme-HFB-based calculations, are beyond the scope of the present study. We left them as future work.

2.1 Helm (top-hat \otimes Gaussian) form factor

The Helm form factor is given by

$$F_{\text{Helm}}(q) = \frac{3 j_1(qR_0)}{qR_0} \exp\left[-\frac{(qs)^2}{2}\right], \quad (7)$$

where R_0 is the diffraction radius that sets the location of the first minimum of the form factor, and s characterizes the surface thickness. The corresponding weak-charge density reads [16]

$$\rho_W(r) = \frac{3Q_W}{8\pi R_0^3} \left\{ \text{erf}\left(\frac{R_0 + r}{\sqrt{2}s}\right) - \text{erf}\left(\frac{r - R_0}{\sqrt{2}s}\right) + \sqrt{\frac{2}{\pi}} \frac{s}{r} \left[e^{-\frac{(r+R_0)^2}{2s^2}} - e^{-\frac{(r-R_0)^2}{2s^2}} \right] \right\}. \quad (8)$$

The rms radius of the weak-charge distribution, the weak radius R_W , is defined as

$$R_W^2 \equiv \frac{\int d^3r r^2 \rho_W(r)}{Q_W}, \quad (9)$$

Isotope	A	r_0 [fm]	Helm		2pF		Primary source
			R_0 [fm]	s [fm]	c [fm]	a [fm]	
C	12	1.20	2.40	0.60	2.355	0.52	[17, 18]
Ca	40	1.20	3.58	0.90	3.593	0.49	[17, 18]
Ca	48	1.20	3.87	0.90	3.670	0.55	[17, 18]
Pb	208	1.20	6.82	0.90	6.624	0.55	[17–19]

Table 1: Nuclear size parameters adopted to construct the weak–charge densities for the target nuclei considered in this work, using the Helm and two–parameter Fermi (2pF) form–factor parametrizations. In the Helm model, the effective diffraction radius R_0 and surface thickness s are chosen to reproduce the corresponding weak rms radius, while the parameter R_0 is introduced solely as a conventional nuclear size scale. For the 2pF parametrization, c and a denote the half–density radius and surface diffuseness, respectively.

which evaluates to

$$R_W^2 = \frac{3}{5} (R_0^2 + 5s^2) \quad (10)$$

for the Helm density. Throughout this work, the characteristic radius appearing in the Helm parametrization is taken as $R = r_0 A^{1/3}$. This quantity should be regarded as an auxiliary nuclear–size scale rather than the weak rms radius itself. The diffraction radius R_0 is then fixed by $R_0^2 = R^2 - 5s^2$ ($R_W = \sqrt{3/5}R$), ensuring a consistent reproduction of the weak radius and the correct placement of diffractive features in the weak form factor.

2.2 Two–parameter Fermi (2pF / Woods–Saxon) form factor

The two–parameter Fermi (2pF) distribution is defined as

$$\rho(r) = \frac{\rho_0}{1 + \exp[(r - c)/a]}, \quad F(q) = \frac{4\pi}{N} \int_0^\infty r^2 \rho(r) j_0(qr) dr. \quad (11)$$

where c and a denote the half–density radius and surface diffuseness, respectively. In CE ν NS applications, the weak form factor closely follows the neutron form factor, with proton contributions suppressed by $(1 - 4 \sin^2 \theta_W)$. By construction, $\int \rho_n(\mathbf{r}) d^3r = N$, and the normalization ensures $F_W(0) = 1$. Physically, $\rho_n(\mathbf{r})$ represents the intrinsic spatial distribution of neutrons, while $F_W(q)$ is the momentum–space quantity directly probed by CE ν NS data.

2.3 Weak–charge densities from Helm and 2pF models

Figure 1 compares the radial weak–charge densities $\rho_W(r)$ obtained with the Helm and 2pF parametrizations for ^{12}C , ^{40}Ca , ^{48}Ca , and ^{208}Pb . All densities are normalized to the total weak charge Q_W (i.e., $\int d^3r \rho_W(r) = Q_W$). Representative parameter sets used for the Helm and 2pF densities are summarized in Table 1.

Across the four nuclei considered, the Helm and 2pF parametrizations reproduce similar overall size scales and surface locations, but they distribute the weak charge differently between the nuclear interior and the surface. In particular, the Helm profile exhibits a flatter and systematically higher core density, whereas the 2pF form has a lower central value and a more gradual decrease from the center. The contrast is most pronounced for the light nucleus ^{12}C and becomes less significant for heavier systems; for ^{208}Pb the two profiles are broadly similar over most of the nuclear volume,

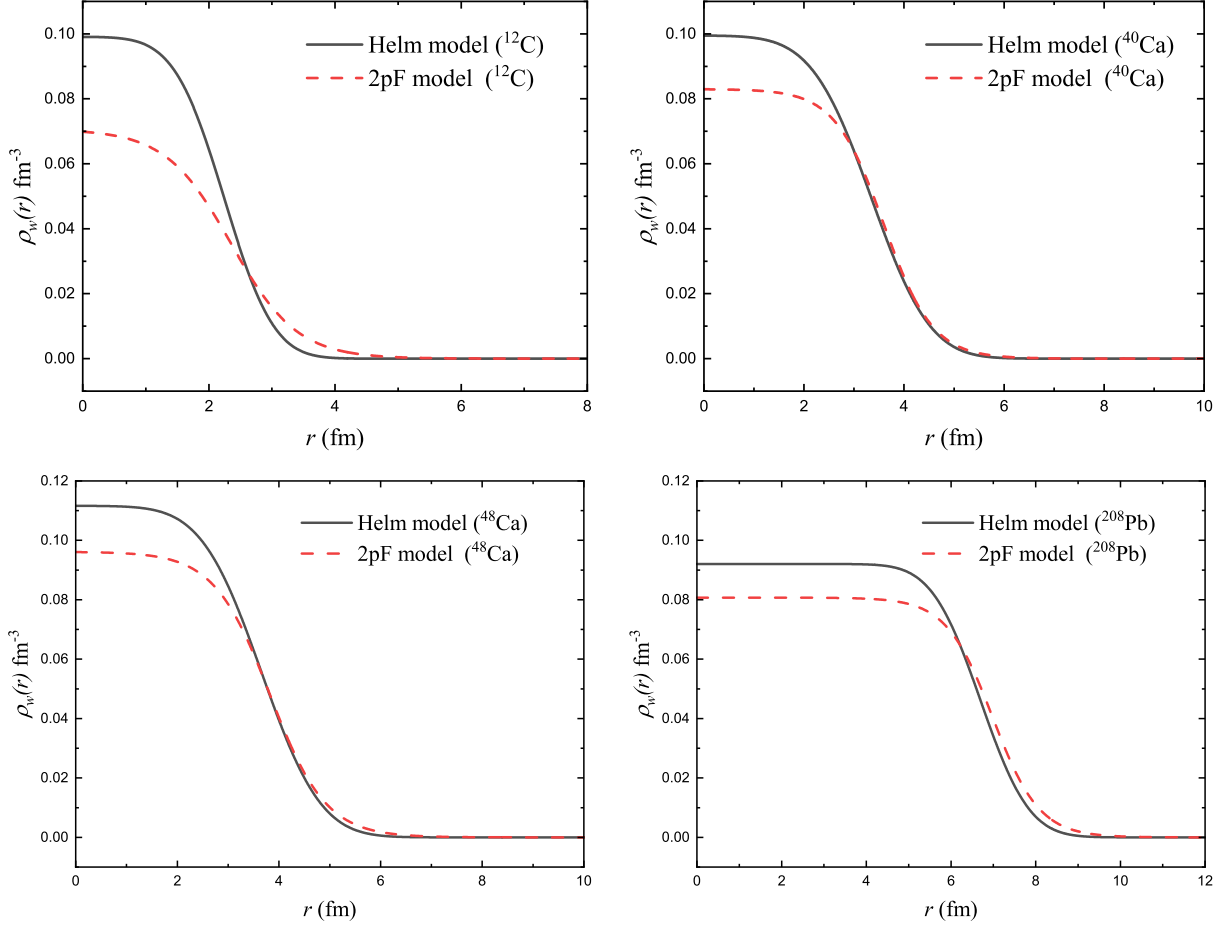


Figure 1: Weak-charge densities $\rho_W(r)$ obtained with the Helm (solid) and two-parameter Fermi (2pF, dashed) parametrizations for ^{12}C , ^{40}Ca , ^{48}Ca , and ^{208}Pb . Each profile is normalized to the total weak charge Q_W (i.e., $\int d^3r \rho_W(r) = Q_W$). The parameter values used in each panel are summarized in Table 1.

with the remaining differences mainly visible in the surface tail at large r . As long as the total weak charge and the low-order radial moments are similar, differences in the core normalization are largely compensated, while surface/tail differences drive the model dependence at intermediate q .

At larger momentum transfer, these surface differences translate into corresponding variations of the weak form factor. In the deeply coherent limit, $qR \ll 1$, the Helm and 2pF models yield nearly identical predictions, while mild model dependence sets in as qR approaches $\mathcal{O}(1)$. Near the first diffraction minimum at $qR \simeq 4.493$, they can induce $\mathcal{O}(10\%)$ shape variations in the predicted recoil spectra for medium-mass nuclei. As the mass number increases, the relevant qR values shift to higher momenta, and the associated model dependence becomes less pronounced. These trends provide a controlled estimate of the theoretical uncertainty associated with weak-density modeling and motivate the use of both parametrizations in the quantitative sensitivity analysis presented below.

2.4 Exact elastic kinematics and experimental access to qR

Experimentally, the momentum transfer is not measured directly. Instead, CE ν NS experiments observe the nuclear recoil energy T and, in some cases, the laboratory scattering angle. For elastic neutrino–nucleus scattering, the recoil energy uniquely fixes the momentum transfer and the scattering angle through

$$q(T) = \sqrt{2MT}, \quad \theta(T) = \arccos\left(1 - \frac{MT}{E_\nu(E_\nu - T)}\right), \quad (12)$$

where M is the nuclear mass and E_ν the incident neutrino energy. This exact kinematical mapping provides a direct link between measured recoil spectra and the momentum–space variables entering the weak form factor.

The maximum recoil energy and the accessible range in qR increase with neutrino energy. Low–energy decay–at–rest sources predominantly probe the coherent regime, with $qR \lesssim 1$ for light and medium–mass nuclei, so that the weak form factor remains close to unity. For heavy targets, $qR > 1$ is reached only near the kinematic endpoint. Higher–energy neutrino sources extend the kinematic reach into the coherent–to–diffractive transition and, for sufficiently heavy targets, approach the vicinity of the first diffractive minimum at $qR \simeq 4.493$. These kinematical considerations clarify the complementary roles of different neutrino sources and provide the foundation for the KDAR–based sensitivity studies presented in the following sections.

Target	A	R [fm]	$E_\nu _{qR=1}$ [MeV]	$E_\nu _{qR=4.493}$ [MeV]	$T^{max} _{qR=1}$ [keV]	$T^{max} _{qR=4.493}$ [MeV]
^{12}C	12	2.747	36	161	~ 229	~ 4.529
^{40}Ca	40	4.104	24	108	~ 23	~ 0.471
^{48}Ca	48	4.361	23	102	~ 23	~ 0.460
^{208}Pb	208	7.110	14	62	~ 2	~ 0.040

Table 2: Representative kinematic energy scales for the target nuclei considered in this work. Shown are the neutrino energies E_ν corresponding to the onset of coherence ($qR \simeq 1$) and to the first diffraction minimum ($qR \simeq 4.493$), together with the associated maximum nuclear recoil energies T^{max} at these kinematic points. The characteristic nuclear radius R entering qR is listed for each target.

2.5 PVES reference points (PREX-II and CREX) on the qR axis

Parity–violating elastic electron scattering (PVES) experiments such as PREX–II and CREX constrain the nuclear weak form factor at essentially a *single* acceptance–averaged momentum–transfer point (i.e. one quoted reference value of $\langle Q^2 \rangle$ or q) [10, 11]. To compare those PVES constraints with the qR systematics used throughout this work, we translate the experimental reference point into the wavenumber q in fm^{-1} and evaluate the corresponding dimensionless products qR (and qR_0 for the Helm diffraction radius).

For a PVES reference point given in terms of the usual spacelike four–momentum transfer $Q^2 \equiv -q^\mu q_\mu$, we locate the point on our qR axis by using

$$q [\text{fm}^{-1}] \equiv \sqrt{\langle Q^2 \rangle}. \quad (13)$$

Strictly speaking, PVES quotes the invariant Q^2 while in CE ν NS kinematics we use the three–momentum transfer $|\mathbf{q}|$; for elastic scattering the energy transfer is small, so this identification is sufficient for the purpose of placing PREX/CREX on the qR axis.

Table 3: PVES momentum–transfer reference points for PREX–II and CREX and their location on the qR axis. The dimensionless products qR and qR_0 are evaluated with $R = r_0 A^{1/3}$ ($r_0 = 1.2$ fm) and the Helm diffraction radius $R_0 = \sqrt{R^2 - 5s^2}$ using the same s values as in Table 1. Experimental reference points and $F_W(q)$ values are taken from Refs. [10, 11].

Experiment	Target	Reference point	q [fm $^{-1}$]	qR	qR_0	$F_W(q)$
PREX–II	^{208}Pb	$\langle Q^2 \rangle = 0.00616$ GeV 2	0.398	2.83	2.71	0.368 ± 0.013
CREX	^{48}Ca	$q = 0.8733$ fm $^{-1}$	0.8733	3.81	3.38	$0.1304 \pm 0.0052 \pm 0.0020$

For qR , we use the same nuclear–size convention as in Table 2, $R = r_0 A^{1/3}$ with $r_0 = 1.2$ fm. For the Helm model, we also quote qR_0 using

$$R_0 = \sqrt{R^2 - 5s^2}, \quad (14)$$

with the same surface thickness s values as in Table 1. The resulting PREX–II and CREX reference points lie in the intermediate window $qR \simeq 3$ –4, i.e. beyond the near–coherent region but still below the first sharp–sphere zero at $qR \simeq 4.493$.

For visual reference, we overlay these PVES points on the corresponding weak form-factor curves in Fig. 2. Because PVES constrains $F_W(q)$ at a single point in this intermediate- qR window, KDAR–driven CE ν NS—which maps a continuous recoil range and can cover comparable qR values—provides a complementary electroweak probe of the same curvature region of the weak form factor.

3 From Coherence to Diffraction: Results for CE ν NS Observables

In this section we present numerical results for the nuclear weak form factors and their impact on coherent elastic neutrino–nucleus scattering (CE ν NS) observables. We first compare the Helm and two–parameter Fermi (2pF) parametrizations at the level of the weak form factor itself, and then examine how these features propagate into recoil spectra for KDAR and pion–decay–at–rest (π DAR) neutrinos. Throughout this section, the emphasis is placed on identifying the kinematic regions in which CE ν NS becomes sensitive to nuclear surface structure beyond overall weak–charge normalization.

3.1 Helm and 2pF weak form factors: from coherence to diffraction

Figure 2 compares the squared weak form factor $F(q)^2$ as a function of the dimensionless variable qR (left panels) and the weak form factor $F(q)$ as a function of the physical momentum transfer q (right panels) for ^{12}C , ^{40}Ca , ^{48}Ca , and ^{208}Pb . Results obtained with the Helm parametrization are shown as solid curves, while those based on the two–parameter Fermi (2pF) form are indicated by dashed curves. Vertical dotted lines mark the locations of the first and second diffractive points of a sharp–sphere density at $qR \simeq 4.493$ and $qR \simeq 7.725$.

3.1.1 Behavior across kinematic regimes

Several generic features are apparent. By construction, both parametrizations satisfy $F(0) = 1$, and they closely coincide in the deeply coherent limit ($qR \ll 1$), where $|F(q)|^2$ remains near unity and model dependence is minimal. As qR increases toward the edge of the coherent window, however, a non-negligible suppression of $|F(q)|^2$ is already visible around $qR \sim \mathcal{O}(1)$, and the onset of this

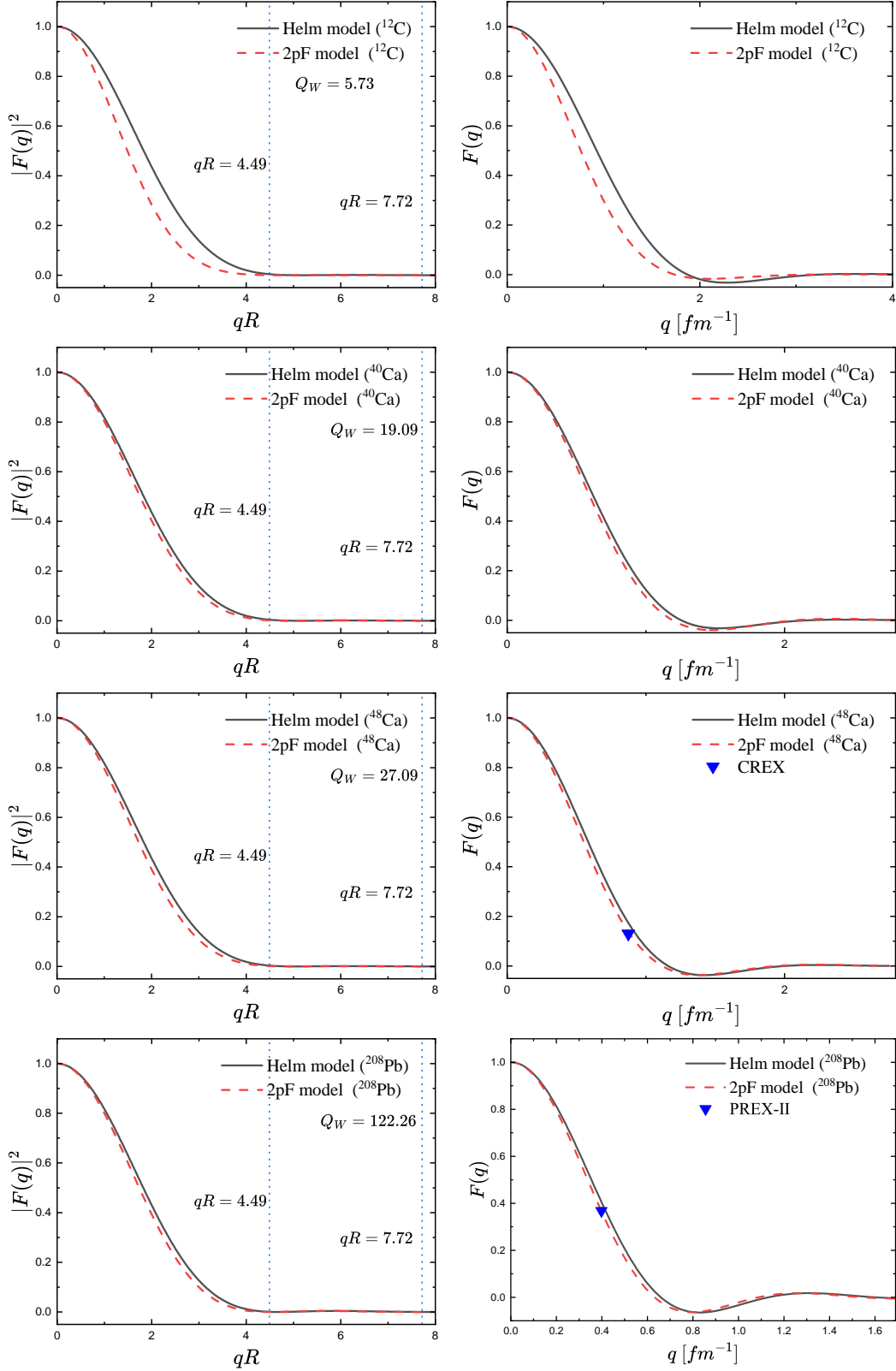


Figure 2: Weak form factors for ^{12}C , ^{40}Ca , ^{48}Ca , and ^{208}Pb calculated with the Helm (solid) and two-parameter Fermi (2pF, dashed) parametrizations. Left panels show $|F(q)|^2$ as a function of qR , and right panels show $F(q)$ as a function of q (in fm^{-1}). Vertical dotted lines indicate the first and second diffraction minima at $qR \simeq 4.493$ and $qR \simeq 7.725$. Markers in the ^{48}Ca and ^{208}Pb right panels indicate the CREX and PREX-II measurements of $F_W(q)$ at their acceptance-averaged momentum transfers (Table 3).

suppression is mildly nucleus dependent (most noticeably for ^{12}C). Thus, $qR \sim 1$ should be regarded as a transition region where form-factor effects begin to contribute, rather than a regime in which $F(q)$ can be treated as strictly unity.

As qR increases further toward the first diffractive minimum (vertical dotted line), both models exhibit the expected rapid damping and the emergence of oscillatory structure. The Helm and 2pF curves remain broadly similar, but small differences develop in the intermediate range and around the depth/location of the minima, reflecting the different surface treatments encoded by (R_0, s) versus (c, a) . For light and medium-mass nuclei, the 2pF curve often lies slightly below the Helm curve over part of the intermediate- qR range, consistent with a smoother surface that suppresses higher-momentum components; for ^{208}Pb the two parametrizations are nearly indistinguishable through the first oscillation, and any residual differences are pushed to larger qR .

The mass dependence is further clarified in the right-hand panels, which display $F(q)$ as a function of the wavenumber q (in fm^{-1}). The first diffractive minimum is determined by the condition $qR \simeq 4.493$, implying $q_{\text{node}} = 4.493/R$. Thus $q_{\text{node}} \propto 1/R$, so that increasing A (and therefore R) shifts the same diffractive feature to smaller values of q and compresses the coherent region into a narrower interval in wavenumber.

3.1.2 Implications for $\text{CE}\nu\text{NS}$ observables

The form-factor features shown in Fig. 2 translate directly into observable effects in $\text{CE}\nu\text{NS}$ recoil spectra through $d\sigma/dT \propto Q_W^2 |F(q(T))|^2$. In the deeply coherent region ($qR \ll 1$), both parametrizations yield nearly identical predictions, so observables are governed primarily by the overall weak-charge normalization. As qR approaches the edge of coherence ($qR \sim 1$) and extends into the intermediate range ($qR \sim 2\text{--}5$), surface-model differences become visible and can induce $\mathcal{O}(5\text{--}15)\%$ variations in the shoulder of the recoil spectrum for light and medium-mass targets. At still larger qR , the absolute rate is already strongly suppressed by $|F(q)|^2$, so residual model differences have limited impact on the total event yield.

These trends indicate that light and medium-mass targets offer the strongest lever arm for probing nuclear surface modeling and neutron density systematics with $\text{CE}\nu\text{NS}$. At the same time, combined analyses involving multiple nuclei can reduce residual form-factor uncertainties in precision extractions, such as constraints on neutron radii, neutron skins, or low-energy tests of the weak mixing angle.

3.2 Recoil kinematics for KDAR and πDAR neutrinos

Figure 3 illustrates how the substantially higher neutrino energy of KDAR ($E_\nu = 236$ MeV) modifies the recoil kinematics relative to pion-decay-at-rest (πDAR , $E_\nu \simeq 30$ MeV) sources. While elastic scattering kinematics uniquely relate recoil energy, momentum transfer, and scattering angle, the higher KDAR energy shifts a significant fraction of events into the region $qR \gtrsim 1$ for light and medium-mass nuclei.

In this kinematic domain, the recoil spectrum is no longer governed solely by the weak-charge normalization but becomes directly sensitive to the shape of the weak form factor and hence to the underlying neutron distribution. By contrast, πDAR kinematics are dominated by the near-coherent regime: for light and medium-mass targets most events satisfy $qR \lesssim 1$, and even for heavy nuclei $qR > 1$ is reached only near the kinematic endpoint. Consequently, $F(q)$ stays close to unity over most of the πDAR recoil range, and direct nuclear-structure sensitivity is intrinsically limited. The higher recoil energies accessible with KDAR further improve robustness against detector thresholds and place the characteristic coherence and diffraction scales at experimentally accessible scattering

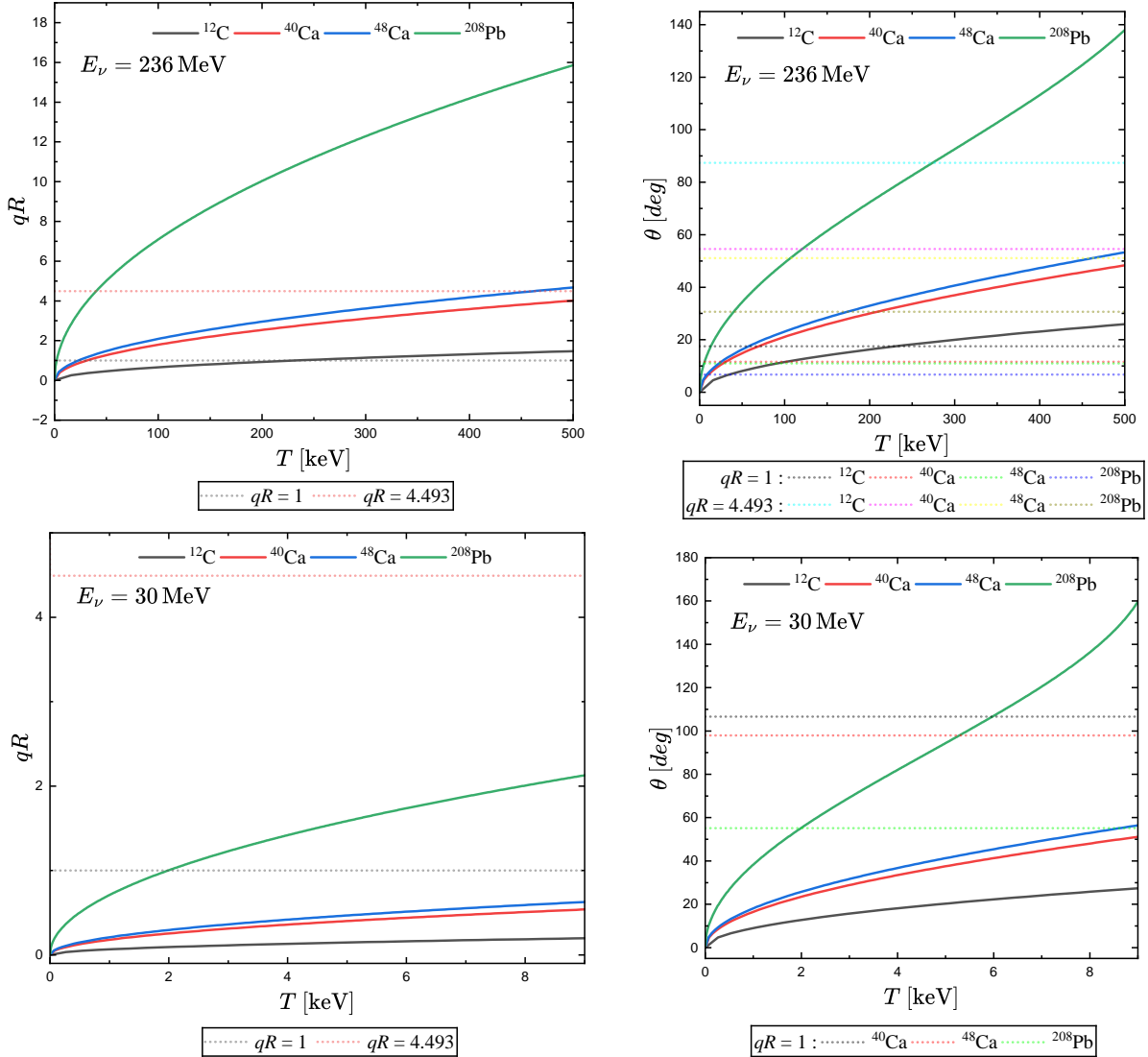


Figure 3: Kinematical comparison of KDAR ($E_\nu = 236$ MeV) and π DAR ($E_\nu \simeq 30$ MeV) neutrinos. Left panels show qR as a function of the recoil energy T for ^{12}C , ^{40}Ca , ^{48}Ca , and ^{208}Pb ; horizontal dashed lines indicate $qR = 1$ and 4.493. Right panels show the corresponding laboratory scattering angle $\theta(T)$; for each target, dashed lines indicate the angles at which $qR = 1$ and 4.493 are reached. KDAR extends the kinematics to larger T and qR , accessing the coherent-to-diffractive transition, while π DAR events are concentrated in the near-coherent region.

angles.

3.3 $\text{CE}\nu\text{NS}$ differential cross sections at KDAR and π DAR

We now turn to the resulting $\text{CE}\nu\text{NS}$ recoil spectra. Figure 4 shows the predicted coherent elastic neutrino-nucleus differential cross sections for ^{12}C , ^{40}Ca , ^{48}Ca , and ^{208}Pb at $E_\nu = 236$ MeV, computed using the Helm and two-parameter Fermi (2pF) parametrizations of the weak form factor. All spectra are evaluated using the leading-order $\text{CE}\nu\text{NS}$ differential cross section introduced in Eq. (1), with the momentum transfer related to the recoil energy by $q = \sqrt{2MT}$ and $M \simeq Am_u$,

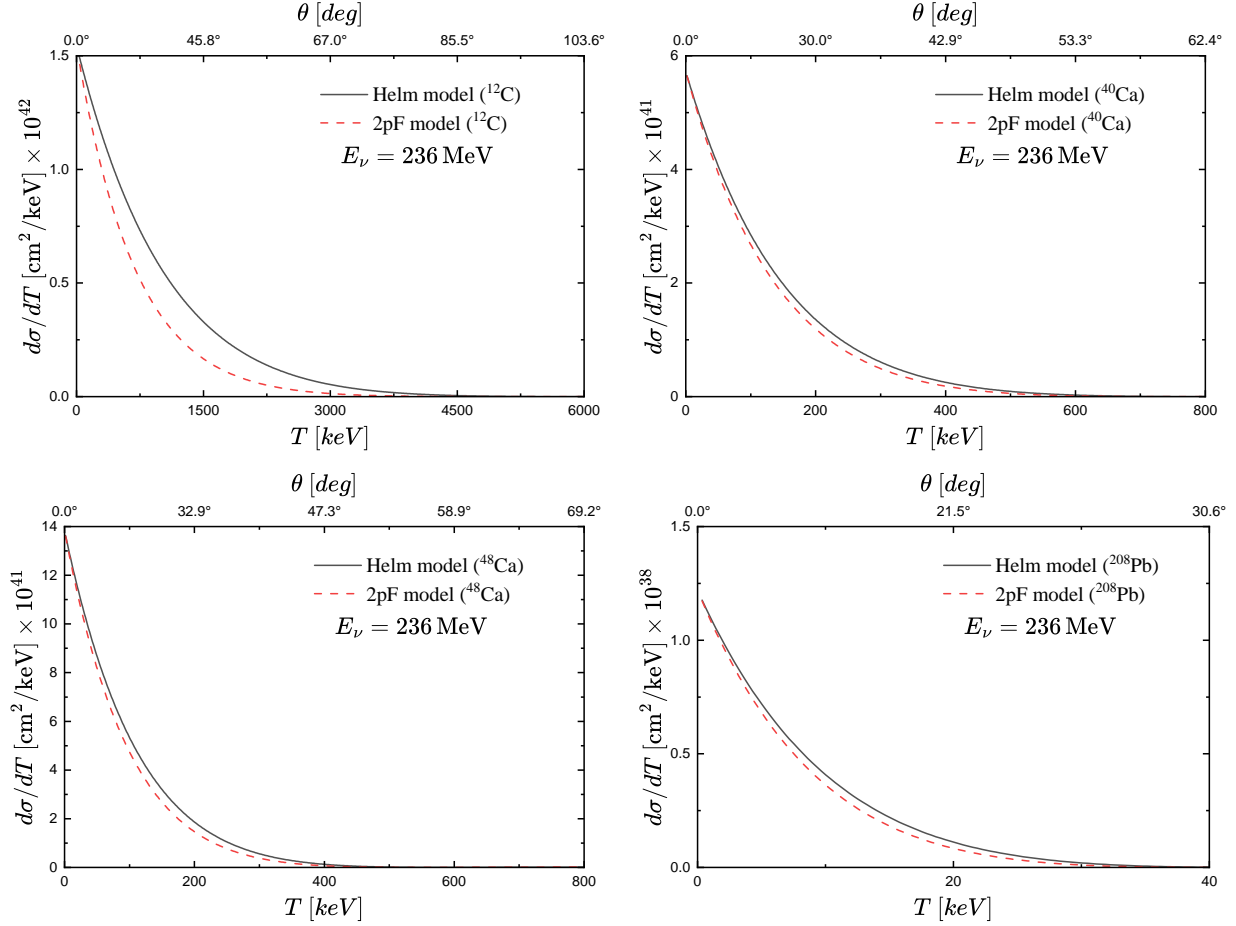


Figure 4: CE ν NS differential cross sections at KDAR ($E_\nu = 236$ MeV) for ^{12}C , ^{40}Ca , ^{48}Ca , and ^{208}Pb , calculated with the Helm (solid) and two-parameter Fermi (2pF, dashed) weak form factors. Upper axes indicate the corresponding laboratory scattering angle. The spectra peak at low recoil energy and decrease rapidly with T ; the overall normalization scales as $Q_W^2 \propto N^2$, while model-dependent differences appear only at larger T , where form-factor suppression becomes significant.

where A is the mass number and m_u is the atomic mass unit. The upper axis in each panel maps the recoil energy T to the corresponding laboratory scattering angle, allowing spectral features to be interpreted equivalently in energy or angle space.

3.3.1 Global trends

For all targets, the recoil spectrum is sharply peaked at low recoil energies and decreases rapidly with increasing T . The overall normalization follows the expected scaling $Q_W^2 \propto N^2$, explaining why ^{208}Pb exhibits the largest differential rate at a given recoil energy despite its smaller kinematic endpoint. Lighter nuclei display broader recoil distributions but with reduced overall normalization.

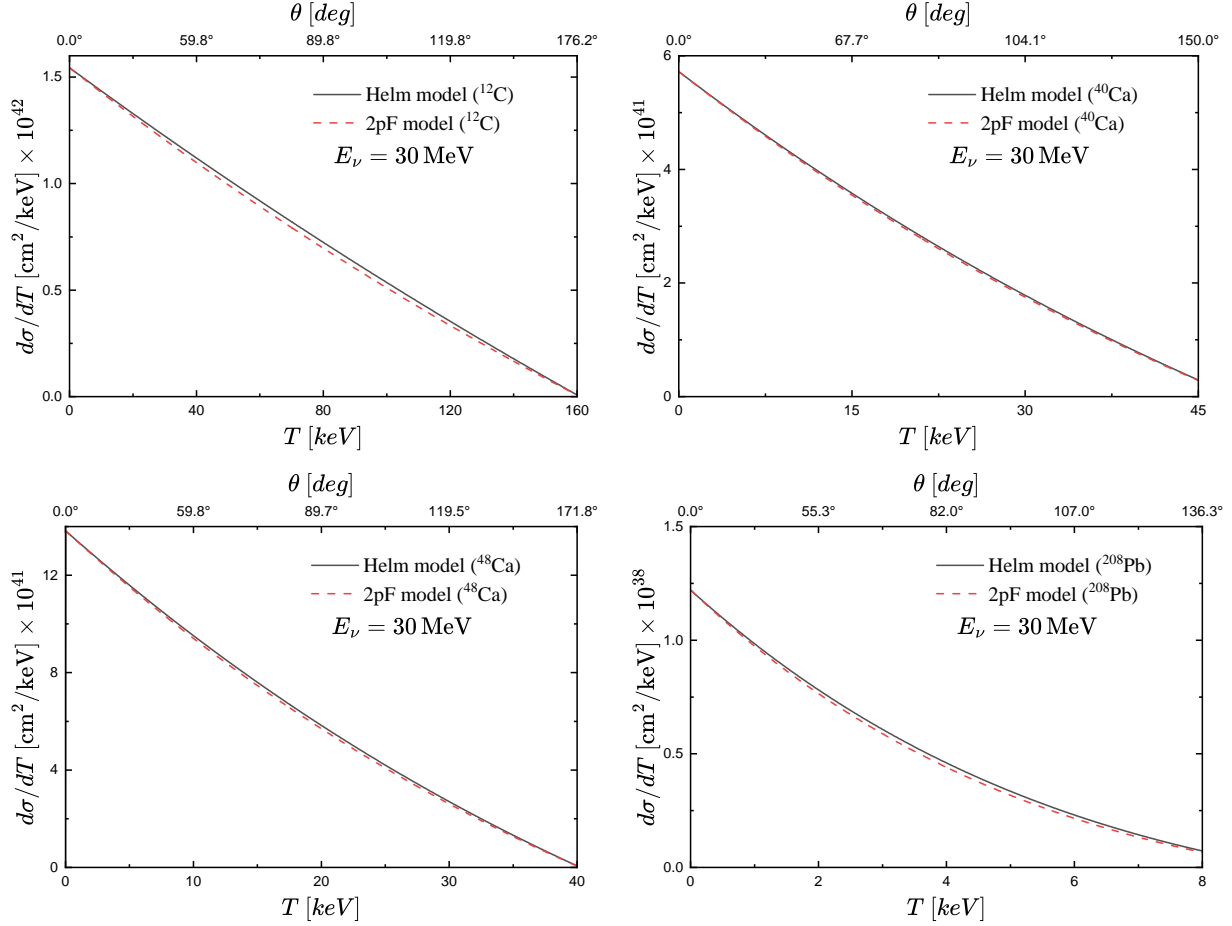


Figure 5: Same as Fig. 4, but for π DAR neutrinos ($E_\nu \simeq 30$ MeV). At these lower energies, the recoil spectra are dominated by the near-coherent region where $F(q) \simeq 1$, and form-factor suppression (and Helm/2pF differences) becomes noticeable only in the high-recoil tail, especially for heavy targets.

3.3.2 Form-factor dependence

At very low recoil energies, where $qR \ll 1$, the Helm and 2pF parametrizations yield indistinguishable spectra because $|F(q)|^2$ remains close to unity. Differences emerge as qR approaches and exceeds unity, where the two models differ slightly in surface curvature and in the depth and location of the first diffractive minimum. At KDAR energies, these effects lead to modest but non-negligible deviations in $d\sigma/dT$ for light and medium-mass nuclei at larger recoil energies, while remaining small in the near-threshold region that dominates the total event rate.

3.3.3 Implications for KDAR versus π DAR

The comparison between KDAR and π DAR recoil spectra is shown in Fig. 5. While both cases share the same low- T rise driven by the weak-charge normalization, the KDAR spectra extend to substantially higher recoil energies and exhibit a progressively stronger suppression from $|F(q)|^2$ as qR approaches and exceeds unity. This is precisely the kinematic region where sensitivity to nuclear surface structure and neutron skins is maximal. By contrast, π DAR spectra are dominated

by the near-coherent regime, where nuclear-structure information is encoded only weakly. Together with the nearly monoenergetic KDAR flux, which avoids the need for spectral unfolding over a Michel distribution, these features make KDAR uniquely well suited for precision CE ν NS studies of neutron radii and neutron skins.

Taken together, the results of this section demonstrate that KDAR-based CE ν NS accesses well-defined kinematic regions in which recoil spectra exhibit genuine sensitivity to the shape of the nuclear weak form factor. While these effects are modest at the level of individual spectra, they arise in a controlled window beyond strict coherence. In the following section, we make this connection quantitative by developing a perturbative framework that relates variations of the weak form factor to the neutron skin thickness.

4 Perturbative interpretation of neutron-skin sensitivity in CE ν NS

The results presented in the previous section demonstrate that KDAR-based CE ν NS accesses kinematic regions in which recoil spectra exhibit genuine sensitivity to the shape of the nuclear weak form factor. In this section, we develop a quantitative and physically transparent framework to interpret these spectral distortions in terms of the neutron skin thickness, $\Delta R_{np} \equiv R_n - R_p$, where R_n and R_p denote the root-mean-square (rms) radii of the neutron and proton distributions, respectively.

Rather than probing the neutron radius directly, CE ν NS is sensitive to the momentum-transfer dependence of the weak form factor $F_W(q)$. Small variations of the neutron distribution modify $F_W(q)$ in a systematic and momentum-dependent manner, particularly beyond the strictly coherent regime. The purpose of this section is therefore to formulate a perturbative description that maps controlled variations of the weak form factor onto variations of ΔR_{np} , thereby clarifying how neutron-surface information is encoded in CE ν NS recoil spectra.

4.1 Neutron dominance and a perturbative expansion of $F_W(q)$

The weak form factor can be written as

$$F_W(q) = \frac{g_p Z F_p(q) + g_n N F_n(q)}{g_p Z + g_n N}, \quad (15)$$

where $F_p(q)$ and $F_n(q)$ are the proton and neutron form factors, and $g_p = \frac{1}{2} - 2 \sin^2 \theta_W$ and $g_n = -\frac{1}{2}$ denote the vector weak couplings. In the Standard Model, using $\sin^2 \theta_W \simeq 0.2386$, the corresponding numerical values are $g_p \simeq 0.023$ and $g_n = -0.5$, indicating that the proton weak coupling is suppressed by more than an order of magnitude relative to the neutron one. Throughout this work, we consistently adopt the low-energy value $\sin^2 \theta_W \simeq 0.2386$, appropriate for CE ν NS kinematics.

It is therefore convenient to characterize the relative proton contribution to the weak form factor by introducing the small, dimensionless expansion parameter

$$\epsilon \equiv \frac{g_p Z}{g_n N}, \quad (16)$$

which measures the ratio of proton to neutron contributions weighted by their weak charges and particle numbers. For the nuclei considered in this work, ϵ is negative and has a magnitude at the level of only a few percent. Numerically, this yields $|\epsilon| \lesssim O(0.05)$ for medium and heavy nuclei.

This confirms that the weak form factor probed in CE ν NS is neutron dominated, while proton contributions enter as a controlled perturbative correction.

Factoring out the dominant neutron contribution, the weak form factor can be rewritten as

$$F_W(q) = \frac{F_n(q) + \epsilon F_p(q)}{1 + \epsilon}. \quad (17)$$

Expanding the denominator and retaining terms up to second order in ϵ , one obtains

$$F_W(q) \simeq F_n(q) - \epsilon [F_n(q) - F_p(q)] + \epsilon^2 [F_n(q) - F_p(q)] \quad (\mathcal{O}(\epsilon^3) \text{ neglected}). \quad (18)$$

This expression makes explicit that the weak form factor probed by CE ν NS is neutron dominated. The leading correction arises at order ϵ and is proportional to the difference between the proton and neutron form factors, while the ϵ^2 term partially cancels the linear contribution. Given that $|\epsilon|$ is at the level of only a few percent for all nuclei considered here, the expansion is rapidly convergent, and proton contributions enter as controlled perturbative corrections.

4.2 From weak form factor variations to neutron-skin variations

The neutron skin thickness enters the weak form factor through the neutron radius, which we parametrize as $R_n = R_p + \Delta R_{np}$. In the following, derivatives with respect to ΔR_{np} are taken at fixed proton rms radius R_p , so that variations of the neutron skin are attributed entirely to changes in the neutron distribution.² This approximation is well justified: R_p is experimentally constrained at the level of ~ 0.01 – 0.02 fm from elastic electron scattering, whereas physically relevant variations of ΔR_{np} are typically $\mathcal{O}(0.1)$ fm. Possible correlated variations of R_p are therefore subleading for CE ν NS and are neglected within the present sensitivity framework.

4.2.1 Low- q mapping and closed-form sensitivities

We first establish an analytic benchmark for neutron-skin sensitivity in the strictly coherent regime, $qR \ll 1$, where the weak form factor admits a controlled low-momentum expansion. Using

$$F_{p,n}(q) = 1 - \frac{q^2}{6} R_{p,n}^2 + \frac{q^4}{120} \langle r^4 \rangle_{p,n} + \mathcal{O}(q^6), \quad (19)$$

and parametrizing the neutron radius as $R_n = R_p + \Delta R_{np}$, the weak form factor expanded up to $\mathcal{O}(q^2)$ can be written as

$$F_W(q) \simeq 1 - \frac{q^2}{6} \left[R_p^2 + 2R_p(1 - \epsilon + \epsilon^2)\Delta R_{np} + (1 - \epsilon + \epsilon^2)(\Delta R_{np})^2 \right] + \mathcal{O}(q^4, \epsilon^3) + \mathcal{O}(q^2(\Delta R_{np})^3). \quad (20)$$

²In nuclear structure models, variations of ΔR_{np} generally imply correlated changes of R_p and R_n . Formally, the CE ν NS response to ΔR_{np} involves a total derivative,

$$\frac{d\mathcal{O}}{d(\Delta R_{np})} = \left(\frac{\partial \mathcal{O}}{\partial \Delta R_{np}} \right)_{R_p} + \left(\frac{\partial \mathcal{O}}{\partial R_p} \right)_{\Delta R_{np}} \frac{dR_p}{d(\Delta R_{np})},$$

corresponding to correlated variations in (R_p, R_n) space. The slope $dR_p/d(\Delta R_{np})$ and the associated covariance are model dependent and not experimentally constrained. We therefore restrict the present analysis to the conditional sensitivity at fixed R_p ; correlated systematics and model comparisons are beyond the scope of this work (see, e.g., Refs. [20, 21]).

Matching Eq. (20) to the standard low- q form $F_W(q) \simeq 1 - q^2 R_W^2/6$ defines the weak-charge radius as

$$R_W^2 = R_p^2 + 2R_p a \Delta R_{np} + a (\Delta R_{np})^2 + \mathcal{O}((\Delta R_{np})^3, \epsilon^3), \quad a \equiv (1 - \epsilon + \epsilon^2). \quad (21)$$

For a reference value $\Delta R_{np}^{(0)}$ and a small shift $\Delta R_{np} = \Delta R_{np}^{(0)} + \delta$, the recoil-spectrum distortion is defined as

$$\Delta_\sigma(T; \delta) \equiv \frac{\left. \frac{d\sigma}{dT} \right|_{\Delta R_{np}^{(0)} + \delta}}{\left. \frac{d\sigma}{dT} \right|_{\Delta R_{np}^{(0)}}} - 1, \quad q = \frac{\sqrt{2MT}}{\hbar c}. \quad (22)$$

The logarithmic sensitivity coefficients,

$$S_1(T) \equiv 2 \frac{\partial}{\partial(\Delta R_{np})} \ln F_W(q) \Big|_{\Delta R_{np}^{(0)}}, \quad S_2(T) \equiv 2 \frac{\partial^2}{\partial(\Delta R_{np})^2} \ln F_W(q) \Big|_{\Delta R_{np}^{(0)}}, \quad (23)$$

can then be evaluated analytically using Eq. (20). Keeping terms consistently up to $\mathcal{O}(q^2)$ yields

$$S_1(T) \simeq -\frac{q^2}{3} a (R_p + \Delta R_{np}^{(0)}) + \mathcal{O}(q^4), \quad (24)$$

and

$$S_2(T) \simeq -\frac{2q^2}{3} a - \frac{2q^4}{9} a^2 (R_p + \Delta R_{np}^{(0)})^2 + \mathcal{O}(q^6), \quad (25)$$

where the $\mathcal{O}(q^4)$ term in S_2 originates from the $(F'_W/F_W)^2$ contribution in $\partial^2 \ln F_W / \partial(\Delta R_{np})^2$.

Exponentiating the logarithmic expansion and retaining terms up to δ^2 , the recoil-spectrum distortion in the coherent regime becomes

$$\Delta_\sigma(T; \delta) = S_1(T) \delta + \frac{1}{2} [S_2(T) + S_1^2(T)] \delta^2 + \mathcal{O}(\delta^3). \quad (26)$$

Substituting Eqs. (24) and (25) and keeping terms up to $\mathcal{O}(q^4 \delta^2)$ yields the explicit closed form

$$\Delta_\sigma(T; \delta) \simeq -\frac{q^2}{3} a (R_p + \Delta R_{np}^{(0)}) \delta - \frac{q^2}{3} a \delta^2 - \frac{q^4}{18} a^2 (R_p + \Delta R_{np}^{(0)})^2 \delta^2 + \mathcal{O}(\delta^3, q^6 \delta^2). \quad (27)$$

Equations (24)–(27) provide a fully analytic description of neutron-skin sensitivity in the strictly coherent regime. They will be used below as a benchmark to assess the breakdown of the low- q approximation and to interpret the numerical results obtained with the full weak form factor at $qR \sim 1$ and in the vicinity of the diffractive minima.

4.2.2 Beyond the coherent limit: sensitivities from the full form factor

The low- q expansion in the previous subsection is not applicable once the momentum transfer enters the diffractive regime. We therefore evaluate the neutron-skin response directly from the full weak form factor.

We use the recoil-spectrum distortion by the exact ratio

$$1 + \Delta_\sigma(T; \delta) = \frac{F_W^2(q; \Delta R_{np}^{(0)} + \delta)}{F_W^2(q; \Delta R_{np}^{(0)})}, \quad (28)$$

where $\Delta R_{np}^{(0)}$ is the reference neutron-skin value and δ is a small shift applied along the one-parameter ΔR_{np} deformation direction. For each shifted value, $F_W(q; \Delta R_{np})$ is recomputed without introducing any approximation in q .

The sensitivity coefficients $S_1(T)$ and $S_2(T)$ are defined as in Eq. (22), but are now evaluated numerically from the full form factor via central differences,

$$\begin{aligned} S_1(T) &\simeq \frac{1}{\delta} \left[\ln F_W(q; \Delta R_{np}^{(0)} + \delta) - \ln F_W(q; \Delta R_{np}^{(0)} - \delta) \right], \\ S_2(T) &\simeq \frac{2}{\delta^2} \left[\ln F_W(q; \Delta R_{np}^{(0)} + \delta) - 2 \ln F_W(q; \Delta R_{np}^{(0)}) + \ln F_W(q; \Delta R_{np}^{(0)} - \delta) \right]. \end{aligned} \quad (29)$$

When desired, $\Delta_\sigma(T; \delta)$ may be related to $S_1(T)$ and $S_2(T)$ through the same second-order expansion already given in Eq. (25). Near diffractive minima, $\Delta_\sigma(T; \delta)$ can be strongly enhanced because the baseline form factor in Eq. (28) is suppressed; however, the absolute rate is simultaneously reduced by the same factor $d\sigma/dT \propto F_W^2(q)$. Consequently, the experimental reach must be assessed by combining the spectral distortion with event statistics, as shown in the numerical results below.

Figure 6 shows the recoil-energy dependence of the fractional spectral distortion $\Delta_\sigma(T; \delta)$ induced by shifting the neutron skin by $\delta = \Delta R_{np} - \Delta R_{np}^{(0)}$, taking $\Delta R_{np}^{(0)} = 0$ [fm] as a reference. The curves correspond to $\delta = \pm 0.01$ fm and ± 0.05 fm and compare the Helm (solid) and 2pF (dashed) parametrizations of the weak form factor.

In the low-recoil (near-coherent) region, $qR \lesssim 1$, the distortion is small and only weakly model dependent. As T increases and the kinematics enter the coherent-to-diffractive transition, $F_W(q)$ departs from unity and the sensitivity grows; pronounced features can occur near recoil energies that map onto diffractive structure of the form factor. These large relative excursions do not necessarily imply a proportionally large experimental reach, because the absolute rate is simultaneously suppressed by the same factor $d\sigma/dT \propto F_W^2(q)$. In contrast, calculations based on the full Helm form factor show pronounced enhancements of Δ_σ at specific recoil energies. These features are associated with diffractive minima of the weak form factor, where $F_W(q)$ approaches zero and the relative cross-section change $\Delta_\sigma(T; \delta) = \sigma(T; \Delta R_{np}^{(0)} + \delta) / \sigma(T; \Delta R_{np}^{(0)}) - 1$ becomes strongly amplified. The positions of these enhancements differ among nuclei, reflecting the dependence of the diffractive pattern on the nuclear size and illustrating how a fixed momentum-transfer condition maps onto different recoil energies for different targets.

It is important to emphasize again that the large values of Δ_σ near diffractive minima do not directly translate into proportionally large experimental sensitivity. In these regions the absolute cross section is strongly suppressed, since $d\sigma/dT \propto F_W^2(q)$ is small, and the available event statistics are limited. The additional panel showing the fractional change obtained from the full form factor alone makes this distinction explicit, separating regions of strong relative sensitivity from those with appreciable event rates.

Overall, Fig. 6 demonstrates that while the low- q expansion reliably captures neutron-skin sensitivity in the strictly coherent regime, it fails to describe the strong, structure-driven enhancements that emerge once the kinematics enter the coherent-to-diffractive transition. This comparison motivates the use of the full weak form factor in the following section, where the recoil-spectrum sensitivity is quantified in terms of experimentally meaningful observables and statistical reach.

4.3 Physical constraints and quantitative sensitivity at KDAR

We now present a quantitative estimate of the neutron-skin sensitivity achievable under realistic KDAR running conditions. The relevant momentum-transfer regimes for each target nucleus have

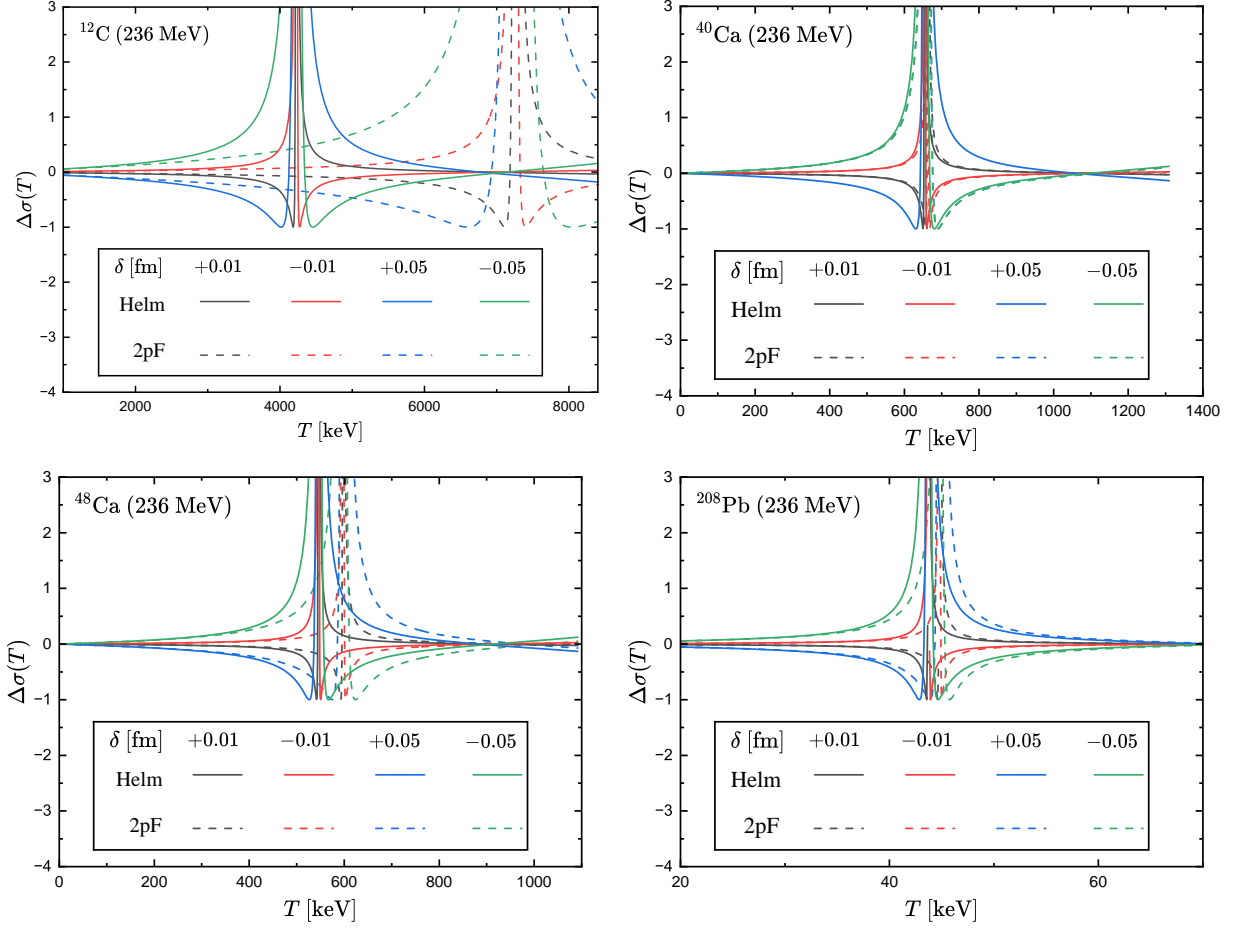


Figure 6: Recoil-energy dependence of the fractional cross-section distortion $\Delta\sigma(T)$ induced by variations of the neutron-skin thickness $\delta = \Delta R_{np} - \Delta R_{np}^{(0)}$ for ^{12}C , ^{40}Ca , ^{48}Ca , and ^{208}Pb in $\text{CE}\nu\text{NS}$ induced by KDAR ν_μ with $E_\nu = 236$ MeV. Results for $\delta = \pm 0.01$ fm and ± 0.05 fm are shown using the Helm (solid) and two-parameter Fermi (2pF, dashed) weak-charge form factors. At low recoil energies the distortion remains small and weakly model dependent, while near diffraction minima of the weak form factor it is strongly enhanced, reflecting the breakdown of the coherent limit. The recoil-energy locations of these enhancement regions depend on the nuclear size, leading to qualitatively different sensitivity patterns among light, medium, and heavy nuclei. This figure illustrates the kinematic localization and physical origin of neutron-skin sensitivity at KDAR energies rather than an optimized experimental observable.

Table 4: Momentum-transfer regimes probed by KDAR neutrinos for the nuclei considered in this work, together with representative experimental constraints on the neutron-skin thickness. The quoted qR ranges indicate the region where the dominant contribution to the event rate arises; access to the first diffractive minimum at $qR \simeq 4.493$ is kinematically possible at KDAR but occurs only in the high-recoil tail where the absolute rate is suppressed.

Nucleus	Dominant qR range	Sensitivity regime	Experimental constraints on ΔR_{np} (fm)
^{12}C	$\lesssim 1$	Near-coherent; form-factor distortions strongly suppressed	No direct neutron-skin constraint
^{40}Ca	~ 1	Coherent-transition region; onset of shape sensitivity	$-0.01^{+0.02}_{-0.02}$ (p-elastic scattering)
^{48}Ca	1-2	Transition to weakly diffractive regime; enhanced sensitivity	0.121 ± 0.026 (exp) ± 0.024 (model) (CREX)
^{208}Pb	2-4	Diffractive regime; strong form-factor modulation	0.283 ± 0.071 (PREX-II)

Table 5: Statistical 1σ sensitivity to the neutron skin thickness ΔR_{np} obtained from the condition $\Delta\chi^2 = 1$ using KDAR-based CE ν NS. We consider representative integrated KDAR fluences at a JSNS²-like facility corresponding to the 2021 dataset [22], the cumulative exposure as of mid-2024 [22], the approved three-year program [23], and an extended five-year exposure³. Here Φ_{KDAR} denotes the time-integrated KDAR ν_μ fluence at the detector location, i.e., the total number of KDAR neutrinos crossing unit area during the considered exposure, quoted in units of cm^{-2} . Unless stated otherwise, the estimates assume a recoil threshold of $T_{\text{th}} = 10$ keV, Gaussian energy smearing with $\sigma_T/T = 10\%/\sqrt{T/\text{MeV}}$, and a total exposure of 10 ton·year.

Exposure Target nucleus \ Φ_{KDAR} [cm^{-2}]	$\Delta R_{np}^{(1\sigma)}$ [fm]			
	2021	mid-2024	3-year	5-year
^{12}C	6.82×10^{11}	2.57×10^{12}	5.85×10^{12}	9.75×10^{12}
^{40}Ca	0.13048	0.06698	0.04420	0.03409
^{48}Ca	0.12063	0.06201	0.04106	0.03167
^{208}Pb	0.09257	0.04749	0.03141	0.02398
	0.06835	0.03489	0.02291	0.01758

already been summarized in Table 4; in this subsection we focus on the numerical sensitivity results themselves, summarized in Table 5.

The sensitivities are organized in terms of the time-integrated KDAR ν_μ fluence at the detector location, Φ_{KDAR} , defined as the total number of KDAR neutrinos crossing unit area during the considered exposure. For a stopped-kaon source, the fluence is obtained from the KDAR neutrino yield per proton on target, the source-to-detector baseline, and the accumulated number of protons on target,

$$\Phi_{\text{KDAR}} = \frac{Y_{\text{KDAR}}}{4\pi L^2} N_{\text{POT}}. \quad (30)$$

In the JSNS² benchmark adopted here, we use a baseline of $L = 24$ m and a KDAR yield $Y_{\text{KDAR}} = 3.8 \times 10^{-3}$ KDAR ν_μ/POT , which corresponds to a fluence per POT of $(\Phi_{\text{KDAR}}/\text{POT}) = 5.25 \times 10^{-11} \text{ cm}^{-2}/\text{POT}$. Using the POT milestones reported by JSNS², this definition leads to the four benchmark fluences employed in Table 5,

$$\Phi_{\text{KDAR}} = 6.82 \times 10^{11}, 2.57 \times 10^{12}, 5.85 \times 10^{12}, 9.75 \times 10^{12} \text{ cm}^{-2}, \quad (31)$$

corresponding to the 2021 dataset [22], the cumulative exposure as of mid-2024 [22], the approved three-year program [23], and an extended five-year,³ respectively.

Table 5 reports the projected statistical 1σ precision $\Delta R_{np}^{(1\sigma)}$ obtained from a binned χ^2 analysis of KDAR-induced recoil spectra, defined by the condition $\Delta\chi^2 = 1$. Unless stated otherwise, the calculation assumes a recoil threshold of $T_{\text{th}} = 10$ keV, Gaussian energy smearing $\sigma_T/T = 10\%/\sqrt{T/\text{MeV}}$, and a total exposure of 10 ton·year; the numerical procedure is detailed in Appendix C. The numerical values in Table 5 provide a fully quantitative statement of the neutron-skin reach attainable with KDAR-based CE ν NS. For the medium-mass nucleus ^{48}Ca , the projected precision improves from $\Delta R_{np}^{(1\sigma)} = 0.0926$ fm at the 2021 benchmark fluence to 0.0240 fm in the extended five-year scenario. This nearly fourfold improvement tracks the increase in Φ_{KDAR} and confirms that the extraction

³The five-year exposure is not quoted as an explicit POT value in the JSNS² documents. Instead, it is obtained by a linear extrapolation of the approved three-year exposure, $N_{\text{POT}} = 1.114 \times 10^{23}$ (corresponding to 1 MW \times 3 years), assuming constant beam delivery. This yields $N_{\text{POT}}^{(5\text{yr})} = (5/3) \times 1.114 \times 10^{23} = 1.857 \times 10^{23}$. The use of a five-year scenario is motivated by the stated long-term operation goal of JSNS² at 1 MW beam power.

remains statistics dominated over the considered exposure range. A similar trend is observed for ^{40}Ca , whose sensitivity closely follows that of ^{48}Ca at all benchmark fluences.

For the heavy nucleus ^{208}Pb , Table 5 shows that precisions at the level of 0.02 fm become attainable as the KDAR fluence accumulates (e.g. 0.0684 fm at the 2021 benchmark improving to 0.0176 fm in the five-year scenario). Although the relative recoil-spectrum distortions induced by neutron-skin variations are enhanced in the diffractive regime for heavy targets, the information is concentrated in the high-recoil tail where the absolute event rate is suppressed. As a consequence, the final statistical precision for ^{208}Pb becomes comparable to, rather than parametrically stronger than, that obtained for the optimal medium-mass target. By contrast, the light nucleus ^{12}C remains intrinsically less constraining. Even at the largest benchmark fluence, the projected uncertainty, $\Delta R_{np}^{(1\sigma)} = 0.0341$ fm, is significantly weaker than for the heavier targets, reflecting the dominance of near-coherent kinematics where neutron-skin effects enter primarily through an overall normalization.

Taken together, Table 5 defines the quantitative experimental parameter space for KDAR-based neutron-skin measurements at a JSNS²-like facility. It demonstrates, in explicitly numerical terms, how the achievable precision on ΔR_{np} scales with accumulated KDAR fluence and identifies medium-mass nuclei, in particular ^{48}Ca , as providing the optimal balance between event statistics and shape sensitivity under realistic detector assumptions.

5 Summary and Conclusions

In this work, we have developed a unified and quantitatively controlled framework that connects nuclear weak-charge densities, weak form factors, and observable CE ν NS recoil spectra across the transition from strict coherence to nuclear diffraction. Focusing on KDAR neutrinos with $E_\nu = 236$ MeV, we have systematically contrasted their kinematic reach with that of conventional pion-decay-at-rest (π DAR) neutrinos and demonstrated the unique advantages of KDAR for probing neutron-skin effects in nuclei. Our analysis spans light, medium-mass, and heavy targets, ^{12}C , ^{40}Ca , ^{48}Ca , and ^{208}Pb , allowing for a coherent comparison across nuclear size.

A central result of this study is that CE ν NS sensitivity to neutron-skin thickness is strongly governed by the dimensionless variable qR . In the strictly coherent regime ($qR \lesssim 1$), nuclear-structure effects are suppressed and neutron-skin variations manifest primarily as overall normalization changes. Meaningful sensitivity emerges only once the kinematics extend into the coherent-to-diffractive transition, where the weak form factor departs from unity and induces genuine, shape-dependent distortions in the recoil spectrum. The vicinity of the first diffractive minimum at $qR \simeq 4.493$ therefore provides a natural benchmark for maximal sensitivity to neutron surface properties.

Using both the Helm and two-parameter Fermi (2pF) parametrizations normalized to the same weak charge, we find that they reproduce comparable overall size scales and surface locations for the nuclei considered, while differing in how the weak charge is distributed between the core plateau and the diffuse surface. Accordingly, the form factors are nearly identical in the deep-coherence limit, but begin to separate once the kinematics enter the coherence-transition region, where recoil spectra acquire genuine shape dependence on the nuclear surface.

These differences remain negligible in the low- q limit yet translate into systematic and physically interpretable spectral distortions once $qR \gtrsim 1$. This observation underscores the necessity of employing the full weak form factor, rather than low- q expansions, when interpreting KDAR-induced CE ν NS spectra.

Exact elastic kinematics further reveal a qualitative contrast between KDAR and π DAR measurements. While π DAR-based CE ν NS remains confined to the near-coherent regime for all nuclei considered, KDAR neutrinos extend the accessible momentum-transfer range into $qR \gtrsim 1$ for light

and medium-mass nuclei and provide access to the diffractive regime for heavier targets. This difference explains why KDAR-based CE ν NS uniquely enables shape-sensitive probes of nuclear structure beyond normalization-only observables.

Building on these physical insights, we have presented a quantitative estimate of the statistical sensitivity to the neutron skin thickness achievable at a JSNS²-like facility. For a total exposure of 10 ton-year and representative integrated KDAR fluences, the projected 1σ sensitivities reach $\Delta R_{np}^{(1\sigma)} \simeq 0.09\text{--}0.02$ fm for ⁴⁸Ca as the fluence increases, while sensitivities for ²⁰⁸Pb approach $\Delta R_{np}^{(1\sigma)} \simeq 0.07\text{--}0.02$ fm. In contrast, lighter nuclei such as ¹²C remain limited by their proximity to the coherent regime. These results demonstrate that KDAR CE ν NS can probe neutron-skin effects through genuine spectral distortions rather than overall rate changes.

In summary, KDAR-based CE ν NS transforms elastic neutrino-nucleus scattering from a predominantly coherent probe governed by weak-charge scaling into a diffraction-sensitive measurement of the nuclear weak form factor. The nearly monoenergetic nature of the KDAR source provides a clean and transparent mapping between momentum transfer, nuclear size, and recoil spectrum distortions, enabling controlled access to neutron surface information. When combined with existing parity-violating electron-scattering results and multi-target analyses, KDAR CE ν NS offers a complementary and electroweakly clean avenue for precision studies of neutron radii and neutron-skin thicknesses in nuclei.

Acknowledgments

This work was supported by the National Research Foundation of Korea (Grant Nos. RS-2022-NR069287, RS-2022-NR070836, RS-2024-00460031, RS-2025-00513410, RS-2025-24533596, and RS-2025-25400847). The work of MKC was supported by the National Research Foundation of Korea (Grant Nos. RS-2021-NR060129 and RS-2025-16071941).

A Elastic kinematics and the variable qR

We summarize the kinematic relations used in the main text for the neutral-current elastic process $\nu(k) + A(P) \rightarrow \nu(k') + A(P')$. We work in the laboratory frame with the target at rest, $P^\mu = (M, \mathbf{0})$, and metric $g^{\mu\nu} = \text{diag}(+, -, -, -)$. The nuclear recoil kinetic energy is $T \equiv P'^0 - M$.

A.1 Momentum transfer and recoil energy

In this Appendix, q^μ denotes the four-momentum transfer, whereas q denotes the corresponding wavenumber in fm^{-1} defined in Eq. (37). Define the four-momentum transfer $q^\mu \equiv k^\mu - k'^\mu = P'^\mu - P^\mu$ and $Q^2 \equiv -q^2 > 0$. Using $P'^2 = P^2 = M^2$, one finds the exact elastic identity

$$m_\ell^2 + 2E_\nu M - 2(E_\nu + M)E'_\nu + 2E_\nu |\mathbf{k}'| \cos\theta = 0, \quad (32)$$

Here θ denotes the scattering angle of the outgoing neutrino, $\cos\theta \equiv \hat{\mathbf{k}} \cdot \hat{\mathbf{k}}'$, and the exact four-momentum transfer

$$|\mathbf{q}|^2 \equiv |(k - k')|^2 = -m_\ell^2 + 2E_\nu E'_\nu - 2E_\nu k' \cos\theta \equiv Q^2. \quad (33)$$

When for a (nearly) massless neutrino ($m_\ell \rightarrow 0$), Eq. (33) reduces to,

$$Q^2 \simeq 2E_\nu E'_\nu (1 - \cos\theta), \quad (34)$$

Eq. (32) reduces to

$$2E_\nu E'_\nu(1 - \cos \theta) \simeq 2MT. \quad (35)$$

So in the heavy-target CEvNS limit (nonrelativistic recoil),

$$Q^2 \simeq 2MT. \quad (36)$$

For CEvNS, we may use the standard approximation $|\mathbf{q}| \simeq \sqrt{2MT}$ when evaluating the weak form factor.

For convenience, the momentum transfer in fm^{-1} is

$$q [\text{fm}^{-1}] \equiv |\mathbf{q}| \simeq \sqrt{2MT}. \quad (37)$$

A.2 Angle–recoil mapping and kinematic endpoint

Combining $E'_\nu = E_\nu - T$ with Eq. (36) and Eq. (34) yields

$$\cos \theta(T) = 1 - \frac{MT}{E_\nu(E_\nu - T)}. \quad (38)$$

Equivalently,

$$T(E_\nu, \theta) = \frac{E_\nu^2(1 - \cos \theta)}{M + E_\nu(1 - \cos \theta)}. \quad (39)$$

The maximum recoil occurs for backward scattering ($\theta = \pi$),

$$T_{\max}(E_\nu, M) = \frac{2E_\nu^2}{M + 2E_\nu}. \quad (40)$$

Inverting Eq. (40), the minimum neutrino energy required to produce a recoil T is

$$E_{\nu, \min}(T) = \frac{1}{2} \left(T + \sqrt{T^2 + 2MT} \right), \quad (41)$$

and the final lepton energy E'_ν is

$$E'_\nu(T, \theta) = \frac{E_\nu}{1 + \frac{E_\nu}{M}(1 - \cos \theta)}. \quad (42)$$

with Eq. (39) and $E'_\nu = E_\nu - T$.

A.3 Dimensionless coherence variable qR and benchmark scales

The degree of coherence is controlled by the dimensionless combination

$$qR \equiv |\mathbf{q}| R \simeq \sqrt{2MT} R, \quad (43)$$

where R is a characteristic nuclear radius (e.g. $R = r_0 A^{1/3}$ with $r_0 \simeq 1.2$ fm, as used for Table 2). This R is introduced only to form the dimensionless variable qR ; the weak form factor itself is computed with its own model parameters (Helm: R_0, s ; 2pF: c, a).

For quick estimates, Eq. (43) gives the characteristic recoil scale at a chosen $qR = x$,

$$T(qR = x) \simeq \frac{x^2}{2MR^2}. \quad (44)$$

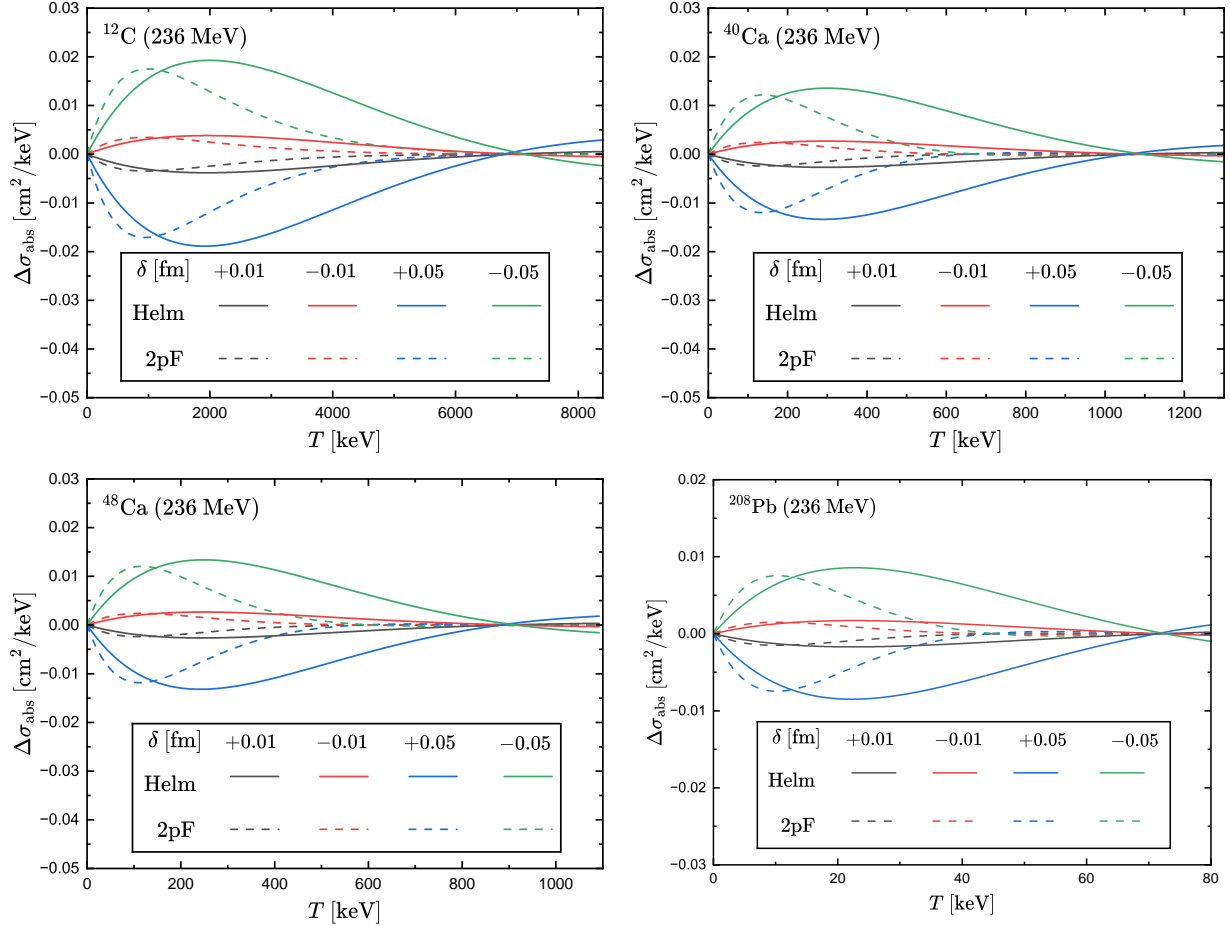


Figure 7: Absolute difference in the CE ν NS differential cross section, $\Delta_{\text{abs}}(T) = d\sigma/dT(T; \Delta R_{np}^{(0)} + \delta) - d\sigma/dT(T; \Delta R_{np}^{(0)})$, for KDAR ν_{μ} with $E_{\nu} = 236$ MeV. Results are shown for ^{12}C , ^{40}Ca , ^{48}Ca , and ^{208}Pb using the Helm (solid) and two-parameter Fermi (2pF, dashed) weak-charge form factors. The absolute scale illustrates the magnitude of the recoil-spectrum variation, complementing the fractional distortion discussed in the main text.

Near the kinematic endpoint (backward scattering) and for $E_{\nu} \ll M$, the neutrino energy that reaches $qR = x$ is approximately

$$E_{\nu}(qR = x) \simeq \frac{x}{2R}, \quad (x = 1, 4.493, \dots). \quad (45)$$

The kinematic endpoint is set by $T_{\text{max}}(E_{\nu}, M)$ in Eq. (40). Separately, diffractive minima arise from the form factor: for a sharp-sphere benchmark the first minimum occurs at $qR \simeq 4.493$ (and the next at $qR \simeq 7.725$), providing a convenient reference scale for maximal form-factor discrimination.

B Absolute cross-section variations induced by neutron-skin changes

In the main text, the sensitivity to neutron-skin variations is illustrated in terms of the fractional distortion of the recoil spectrum, which highlights the intrinsic dependence on the nuclear weak form factor. To complement this representation, Fig. 7 shows the corresponding absolute difference

in the differential cross section,

$$\Delta\sigma_{\text{abs}}(T) = \frac{d\sigma}{dT}(T; \Delta R_{np}^{(0)} + \delta) - \frac{d\sigma}{dT}(T; \Delta R_{np}^{(0)}), \quad (46)$$

for $\delta = \pm 0.01$ fm and ± 0.05 fm.

As expected, the absolute difference remains finite and smooth across the entire recoil-energy range, including the vicinity of diffractive minima where the fractional distortion exhibits pronounced enhancements. This behavior reflects the fact that, although the relative sensitivity is maximized near form-factor nodes, the cross section itself is suppressed in these regions. The results therefore indicate the characteristic scale of the event-rate variation associated with neutron-skin changes, without implying an optimized experimental sensitivity.

C Numerical procedure for the sensitivity estimates

This Appendix briefly summarizes the numerical procedure used to obtain the target-dependent neutron-skin sensitivities reported in Table 5. The aim is to document the concrete numerical pipeline employed in the calculations, rather than to repeat the analytic formalism discussed in the main text.

C.1 Binned event prediction with detector response

For each target nucleus, we construct the recoil-energy spectrum induced by monoenergetic KDAR neutrinos at $E_\nu = 236$ MeV. For a given neutron-skin thickness ΔR_{np} , the unsmearred differential event rate per unit KDAR fluence is written as

$$\frac{dN}{dT}(T; \Delta R_{np}) = N_T \frac{d\sigma}{dT}(T; \Delta R_{np}), \quad (47)$$

where N_T is the number of target nuclei corresponding to the assumed exposure. The CE ν NS differential cross section includes the full weak form factor and is evaluated using a fixed low-energy effective weak mixing angle, $\sin^2 \theta_W(Q^2 \simeq 0) = 0.2386$, appropriate for neutral-current processes at momentum transfers $Q \sim \mathcal{O}(10\text{--}100)$ MeV.

Detector effects are incorporated through a Gaussian energy-resolution model. Rather than performing nested numerical integrations for each recoil bin, the smearing is implemented by constructing a detector response matrix, R_{ik} , which gives the probability for an event with true recoil energy T_k to be reconstructed in the observed recoil bin $[T_i, T_{i+1}]$. The expected number of events per unit fluence in bin i is then obtained as

$$N_i(\Delta R_{np}) = \sum_k R_{ik} \frac{dN}{dT}(T_k; \Delta R_{np}) \Delta T, \quad (48)$$

where ΔT is the spacing of the discretized true-energy grid. This approach avoids repeated adaptive integrations and allows for an efficient evaluation of binned spectra over a wide range of ΔR_{np} values.

C.2 Extraction of the 1σ sensitivity

To quantify the statistical sensitivity to the neutron-skin thickness, binned predictions at a trial value ΔR_{np} are compared to a reference spectrum computed at $\Delta R_{np}^{\text{ref}}$. Assuming Poisson statistics

and neglecting systematic uncertainties, we define

$$\Delta\chi^2(\Delta R_{np}) = \sum_i \frac{[N_i(\Delta R_{np}) - N_i(\Delta R_{np}^{\text{ref}})]^2}{N_i(\Delta R_{np}^{\text{ref}})}. \quad (49)$$

Since the event counts scale linearly with the integrated KDAR fluence, $\Delta\chi^2$ is first computed per unit fluence and subsequently rescaled to the benchmark fluence quoted in Table 5. The 1σ sensitivity is obtained by solving $\Delta\chi^2(\Delta R_{np}) = 1$ in the vicinity of $\Delta R_{np}^{\text{ref}}$ using a one-dimensional root search.

C.3 Numerical settings and stability checks

All numerical evaluations were performed in `Mathematica` using a fixed discretization of the true recoil energy with step size ΔT , chosen to balance numerical efficiency and accuracy. The resulting sensitivities were verified to be stable against moderate variations of the true-energy step size and recoil-energy bin width. The procedure described above reproduces the values reported in Table 5 and provides a transparent and computationally efficient framework for the sensitivity estimates presented in this work.

References

- [1] D. Akimov *et al.* (COHERENT Collaboration), *Science* 357, 1123 (2017).
- [2] D. Akimov *et al.* (COHERENT Collaboration), *Phys. Rev. Lett.* 126, 012002 (2021).
- [3] S. Adamski *et al.* (COHERENT Collaboration), *Phys. Rev. Lett.* 134, 231801 (2025), arXiv:2406.13806 [hep-ex].
- [4] N. Ackermann *et al.* (CONUS+ Collaboration), *Nature* 643, 1229–1233 (2025).
- [5] E. Aprile *et al.* (XENON Collaboration), *Phys. Rev. Lett.* 133, 191002 (2024), arXiv:2408.02877 [nucl-ex].
- [6] Z. Bo *et al.* (PandaX Collaboration), *Phys. Rev. Lett.* 133, 191001 (2024).
- [7] O. Tomalak *et al.*, *Prog. Part. Nucl. Phys.* 129, 104019 (2023).
- [8] A. Cadeddu *et al.*, *Phys. Rev. C* 100, 015807 (2019).
- [9] J. Billard, J. Johnston and B. J. Kavanagh, *JCAP* 11, 016 (2018), arXiv:1805.01798 [hep-ph].
- [10] D. Adhikari *et al.* (PREX Collaboration), *Phys. Rev. Lett.* 126, 172502 (2021).
- [11] D. Adhikari *et al.* (CREX Collaboration), *Phys. Rev. Lett.* 129, 042501 (2022).
- [12] J. Birkhan *et al.*, *Phys. Rev. Lett.* 118, 252501 (2017).
- [13] A. Tamii *et al.*, *Phys. Rev. Lett.* 107, 062502 (2011).
- [14] T. Miyatshu *et al.*, *Symmetry* 17, 1872 (2025).
- [15] D. Z. Freedman, *Phys. Rev. D* 9, 1389 (1974).

- [16] C. J. Horowitz *et al.*, Phys. Rev. C 85, 032501(R) (2012).
- [17] H. de Vries, C. W. de Jager and C. de Vries, At. Data Nucl. Data Tables 36, 495–536 (1987).
- [18] I. Angeli and K. P. Marinova, At. Data Nucl. Data Tables 99, 69–95 (2013).
- [19] A. B. Jones and B. A. Brown, Phys. Rev. C 90, 067304 (2014).
- [20] S. Kim *et al.*, Phys. Rev. C 105, 034340 (2022), arXiv:2112.06520 [nucl-th].
- [21] M. H. Mun *et al.*, Phys. Rev. C 110, 014314 (2024), arXiv:2402.19210 [nucl-th].
- [22] E. Marzec *et al.* (JSNS² Collaboration), Phys. Rev. Lett. 134, 081801 (2025), arXiv:2409.01383 [hep-ex].
- [23] S. Ajimura *et al.* (JSNS² Collaboration), arXiv:2012.10807 [hep-ex].